Parametric Analysis of Fischer-Tropsch Synthesis in a Catalytic Microchannel Reactor

Gamze Gumuslu and Ahmet K. Avci
Dept. of Chemical Engineering, Bogazici University, Bebek 34342, Istanbul, Turkey

DOI 10.1002/aic.12558
Published online March 2, 2011 in Wiley Online Library (wileyonlinelibrary.com).

Fischer-Tropsch synthesis (FTS) involves highly exothermic conversion of syngas to a wide range of hydrocarbons, but demands isothermal conditions due to the strong dependence of product distribution on temperature. Running FTS in microchannel reactors is promising, as the sub-millimeter dimensions can lead to significant intensification that inherently favors robust temperature control. This study involves computer-based FTS simulations in a heat-exchange integrated microchannel network composed of horizontal groups of square-shaped cooling and wall-coated, catalytic reaction channels. Effects of material type and thickness of the wall separating the channels, side length of the cooling channel, coolant flow rate, and channel wall texture on reaction temperature are investigated. Use of thicker walls with high thermal conductivities and micro-baffles on the catalytic reaction channel wall favor near-isothermal conditions. Response of reaction temperature against coolant flow rate is significant. Using cooling channels with smaller side lengths, however, is shown to be insufficient for temperature control. © 2011 American Institute of Chemical Engineers *AIChE J,* 58: 227–235, 2012

Keywords: Fischer-Tropsch synthesis, heat-exchange reactor, microchannel reactor, modeling, temperature control

Introduction

Crude oil is an important commodity as it has been used in energy generation as a fuel and in the production of many chemicals as a raw material. However, as the price of crude oil is unstable and its natural resources are becoming depleted, production of synthetic fuels by Fischer-Tropsch synthesis (FTS) is becoming more important.[1,2] FTS is a collection of reactions which converts synthesis gas, a mixture of CO and H_2, to a wide range of hydrocarbons such as paraffins, olefins, and oxygenates in the presence of iron, cobalt, or ruthenium catalysts.[3,4] As synthesis gas generation does not depend on petroleum and can be produced from natural gas, coal, or biomass, FTS offers an alternative, petroleum-free route to produce commodity fuels such as gasoline and diesel.[5]

Success of FT operation is strongly linked to the ability of obtaining desired product selectivity in terms of type and chain length of the hydrocarbons, which are strongly affected by the process conditions, namely by temperature, partial pressures of H_2 and CO in feed and space velocity.[6] It is confirmed by many studies in the literature that the impact of process temperature on selectivity is more significant than those of other operating conditions.[2–4] Therefore, to obtain hydrocarbons in the desired type and carbon-number range, it is essential to have robust temperature control over the FT process. A novel way of meeting this important requirement is through the use of microchannel reactors, the units involving flow paths with characteristic dimensions in the 10^{-4} to 10^{-3} m range, which can lead to very high surface area to volume ratios up to ~50,000 m^2/m^3.[7,8] Microchannel units are usually made of metallic substrates

Correspondence concerning this article should be addressed to A. K. Avci at avciahme@boun.edu.tr.

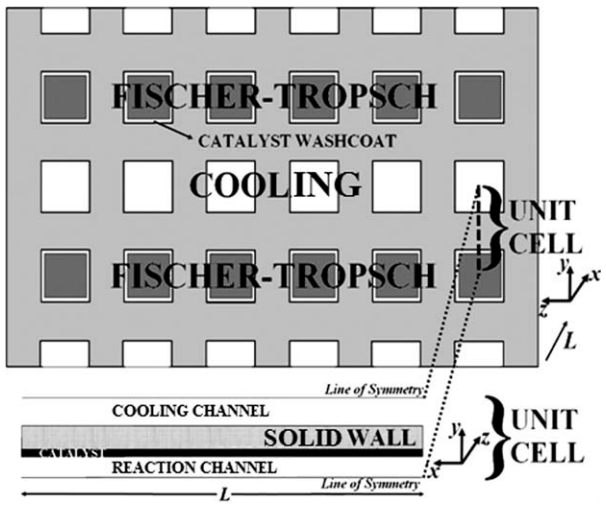

Figure 1. Heat-exchange integrated microchannel reactor system and the unit cell.

and catalysts are generally in the form of thin layers coated on the inner walls of the channels. Combination of these features ends up with very high rates of heat transfer allowing robust temperature control and the resulting uniform temperature distribution throughout the reactor helps in efficient use of the catalyst. Moreover, small channel volumes ensure inherent safety, while well-defined micro-flow paths lead to narrow and low residence time distribution.[8,9]

Combining the advantages of microchannel technology with the requirements of FTS has been addressed by several groups. Cao et al.[10] combined the effective heat removal and improved mass transfer characteristics of microchannel reactors with FTS and evaluated the catalyst performance. They also modeled the reaction system to explore the effects of pressure and molar hydrogen-to-carbon monoxide ratio on the microreactor behavior.[10] Guillou et al.[11] studied splitting hydrogen feed through a staged FTS microreactor system to observe its effects on CO conversion and on product distribution. Myrstad et al.[12] tested cobalt-catalyzed FTS in a microstructured reactor in which exothermal heat is removed effectively by oil flowing in cross-flow channels placed adjacent to the structured catalyst foils. Arzamendi et al.[13] investigated three-dimensional modeling and simulation of a microchannel reactor system in which channels involving low temperature FT reactions are coupled with cooling channels to analyze the conditions to keep the FT temperature at near isothermal conditions. In their study, cross-flow of the streams was considered and the effects of system pressure and the coolant flow rate on temperature were examined.[13]

The aim of this work is to investigate the response of FTS temperature in a heat-exchange integrated microchannel reactor against changes in the geometric configurations and in operating conditions through a series of computer-based parametric analyses. The reactor system, shown in Figure 1 and explained in the next section, is considered to be a microchannel network composed of adjacent channels in the form of parallel arrays, which are arranged such that the coolant and reaction mixtures flow in successive flow paths. Parametric study is conducted through changing the material and thickness of the wall separating cooling and reaction channels, side length of the cooling channel, superficial velocity of the cooling fluid, and channel wall texture for the purpose of figuring out the impact of each parameter on FTS temperature. Results are obtained by the simultaneous solution of the momentum, mass, and energy transport equations using the finite element method under COMSOL Multiphysics^{TM} platform and are presented in the "Results and Discussion" section.

Modeling of the Microchannel Reactor System

The microchannel reactor system, presented in Figure 1, is composed of parallel coupling of square-shaped reactor and cooling channels, which are separated by a solid wall. Inner walls of the reaction (FTS) channels are considered to be coated with a porous, iron-based catalyst layer, forming the washcoat domain. However, the cooling channels are noncatalytic, serve as heat sinks to absorb the heat released from the exothermic FT reactions, and involve the flow of steam as the cooling fluid in the direction counter-current to that of reactive flow. As properties of the fluids flowing within the channels of the same (horizontal) group do not differ, it is assumed that heat transfer between the channels of the same group (i.e., in z-direction) is negligible compared with heat flow between the channels of different groups (i.e., in y-direction). Therefore, any kind of gradients in the z-direction is eliminated. This simplification allows the calculations to be based on a two-dimensional unit cell, which is made up of the domain between the centerlines of two channels through the channel length, as shown in Figure 1. The repeating pattern of the channels in the y-direction, and the resulting symmetry allows the consideration of the half-channel heights in the unit cell, which is the characteristic unit of the multichannel unit.

In this study, the FTS is considered to run at the high temperature mode over an iron-based catalyst. Olefin and paraffin production (Reactions 1 and 2) and water–gas shift (WGS) (Reaction 3) are treated as the only reactions taking place in the reaction channel, discarding any side reactions producing alcohols and ketones:

$$n\mathrm{CO} + (2n+1)\mathrm{H_2} = \mathrm{C}_n\mathrm{H}_{2n+2} + n\mathrm{H_2O} \qquad (n \geq 1) \qquad (1)$$

$$n\mathrm{CO} + 2n\mathrm{H_2} = \mathrm{C}_n\mathrm{H}_{2n} + n\mathrm{H_2O} \qquad (n \geq 2) \qquad (2)$$

$$\mathrm{CO} + \mathrm{H_2O} = \mathrm{CO_2} + \mathrm{H_2} \qquad -\Delta H_{298\ \mathrm{K}} = 41.2\ \mathrm{kJ/mol} \qquad (3)$$

In Reactions (1) and (2), the maximum carbon number is taken as 7 for ensuring that no condensation occurs in the reaction channels; the C_1–C_7 range is mainly composed of fuel gas, LPG and gasoline.[4] CO_2 and H_2O are other products formed by the synthesis reactions. H_2, which is a constituent of the feed, is also produced by the WGS. Inlet temperatures of the feeds to the reaction and cooling channels are taken as 623 K and 374 K, respectively, and the minimum temperatures in all simulations are observed to be around 600 K. The inlet pressure of synthesis gas is taken as 2×10^6 Pa, whereas steam is fed at atmospheric pressure to the cooling channel. In order to test the status of liquid phase formation in the reaction channel, a mixture of reactants and products with suitable compositions is simulated to pass through a microchannel at temperature and pressure specified above using ChemCAD^{TM} process simulator.

Table 1. Model Equations Used to Describe Transport and Reaction in Microchannels

Fluid phase	
Equation of continuity	$\frac{\partial v_{x,i}}{\partial x_i}+\frac{\partial v_{y,i}}{\partial y_i}=0$
Equations of motion	$\rho_{\mathrm{f},i}\left(v_{x,i}\frac{\partial v_{x,i}}{\partial x_i}+v_{y,i}\frac{\partial v_{x,i}}{\partial y_i}\right)=-\frac{\partial p_i}{\partial x_i}+\mu_i\left(\frac{\partial^2 v_{x,i}}{\partial x_i^2}+\frac{\partial^2 v_{x,i}}{\partial y_i^2}\right)$
	$\rho_{\mathrm{f},i}\left(v_{x,i}\frac{\partial v_{y,i}}{\partial x_i}+v_{y,i}\frac{\partial v_{y,i}}{\partial y_i}\right)=-\frac{\partial p_i}{\partial y_i}+\mu_i\left(\frac{\partial^2 v_{y,i}}{\partial x_i^2}+\frac{\partial^2 v_{y,i}}{\partial y_i^2}\right)$
Equation of species continuity	$v_{x,1}\frac{\partial c_{j,1}}{\partial x_1}+v_{y,1}\frac{\partial c_{j,1}}{\partial y_1}=D_{AB,1}\left(\frac{\partial^2 c_{j,1}}{\partial x_1^2}+\frac{\partial^2 c_{j,1}}{\partial y_1^2}\right)$
Equation of energy	$\rho_{\mathrm{f},i}C_{\mathrm{Pf},i}\left(v_{x,i}\frac{\partial T_i}{\partial x_i}+v_{y,i}\frac{\partial T_i}{\partial y_i}\right)=k_{\mathrm{f},i}\left(\frac{\partial^2 T_i}{\partial x_i^2}+\frac{\partial^2 T_i}{\partial y_i^2}\right)$
Catalytic washcoat phase	
Equation of continuity	$\frac{\partial v_{x,1}}{\partial x_1}+\frac{\partial v_{y,1}}{\partial y_1}=0$
Equations of motion	$\left(\frac{\mu_1}{\kappa}\right)v_{x,1}=-\frac{\partial p_1}{\partial x_1}+\left(\frac{\mu_1}{\varepsilon_{\mathrm{p}}}\right)\left(\frac{\partial^2 v_{x,1}}{\partial x_1^2}+\frac{\partial^2 v_{x,1}}{\partial y_1^2}\right)$
	$\left(\frac{\mu_1}{\kappa}\right)v_{y,1}=-\frac{\partial p_1}{\partial y_1}+\left(\frac{\mu_1}{\varepsilon_{\mathrm{p}}}\right)\left(\frac{\partial^2 v_{y,1}}{\partial x_1^2}+\frac{\partial^2 v_{y,1}}{\partial y_1^2}\right)$
Equation of species continuity	$v_{x,1}\frac{\partial c_{j,1}}{\partial x_1}+v_{y,1}\frac{\partial c_{j,1}}{\partial y_i}=D_{AB,\mathrm{eff}}\left(\frac{\partial^2 c_{j,1}}{\partial x_1^2}+\frac{\partial^2 c_{j,1}}{\partial y_1^2}\right)+\rho_{\mathrm{s}}R_{j,1}$
Equation of energy	$\rho_{\mathrm{s}}C_{\mathrm{Ps}}\left(v_{x,1}\frac{\partial T_1}{\partial x_1}+v_{y,1}\frac{\partial T_1}{\partial y_1}\right)=k_{\mathrm{eff}}\left(\frac{\partial^2 T_1}{\partial x_1^2}+\frac{\partial^2 T_1}{\partial y_1^2}\right)+\rho_{\mathrm{s}}\sum_{m=1}^{N}(-\Delta H_m)(r_m)$
Solid wall phase	
Conservation of energy	$k_{\mathrm{w}}\left(\frac{\partial^2 T_{\mathrm{w}}}{\partial x_{\mathrm{w}}^2}+\frac{\partial^2 T_{\mathrm{w}}}{\partial y_{\mathrm{w}}^2}\right)=0$

Outcomes of this simulation verifies that liquid-phase formation does not occur in the reaction channel. Similarly, condensation does not take place in the cooling channel, as steam fed just above its boiling point will be heated further by the exothermic FT reactions. Based on these facts, construction of the mathematical model is based on gas–solid type of operation with fluid (gas) and washcoat (catalyst) phases.

Modeling of the simultaneous reaction and cooling in the unit cell configuration requires the consideration of equation of continuity together with momentum, energy, and species mass conservation equations for the three domains, namely, the fluid phase, the catalytic washcoat phase, and the solid wall phase. Reactor geometry is represented and model equations are set using Cartesian coordinates. It is assumed that the reactions occur only in the washcoat domain, i.e., there is no reaction taking place in fluid phase. The fluids are assumed to be of incompressible Newtonian type and are treated to behave ideally. The entire operation is considered to be at the steady state. The resulting mass, momentum, and energy conservation equations used in modeling are given in Table 1. Conservation of momentum for the gas phase is described by Navier-Stokes equations including contributions of diffusive and convective mechanisms, whereas Brinkman-type equations are used to model flow in the porous washcoat domain. Permeability and porosity of the washcoat layer are taken as 1×10^{-8} m^2 and 5×10^{-1}, respectively.[14,15] The fluid in the reaction channel is characterized by the CO-H_2 mixture and, based on this assumption, thermal conductivity, viscosity, density, specific heat capacity, and diffusivity are calculated as functions of temperature using the mixing laws and correlations reported in the literature.[16–18] Thermal conductivity of the fluid within the catalytic washcoat phase is taken as 4.5 times the bulk fluid conductivity.[14] Effective diffusivity within the porous catalyst layer is calculated from binary diffusivity by taking tortuosity, taken as 4, and porosity of the catalyst into account.[15,19] Kinetic expressions of Langmuir-Hinshelwood type that are used for describing FT synthesis over a Fe-Cu-K catalyst are adapted from the study of Wang et al.[20] The proposed rate expressions, presented in Table 2, involve separate terms for rates of formation of CH_4, C_{2+} alkanes, and alkenes, and for WGS that runs as a side reaction and also terms for the chain growth probability. In contrast with the Anderson-Schulz-Flory distribution, the growth probability terms include chain growth factor related to the carbon number.[20]

Model equations presented in Table 1 are solved subject to the boundary conditions given in Table 3. No-slip condition is used on the channel walls. Concentrations of the species are specified at the inlet boundaries, and convective fluxes defined at the exit are taken as zero. Similarly, for energy conservation equations, boundary conditions at the exit are assumed to be of convective type and set as zero. Heat transfer between the solid wall and the fluid flowing in porous washcoat is handled by means of heat flux continuity at the interface. The model equations constituting a set of partial differential equations are solved using the finite element method under the COMSOL Multiphysics™ platform. Code executions are run on a HP xw8600 workstation with 4×2.00 GHz processors and 16 GB of memory. Unstructured meshing is used with ~41,500

Table 2. Rate Expressions Used in Simulations (Adapted from Wang et al.[20])

$$r_{CH_4} = \frac{k_{AM} P_{H_2} \alpha_1}{1 + \left(1 + \frac{1}{K_a K_b K_c}\frac{P_{H_2O}}{P_{H_2}} + \frac{1}{K_b K_c}\frac{1}{P_{H_2}} + \frac{1}{K_c}\right) \sum_{m=1}^{N} \left(\prod_{j=1}^{m} \alpha_j\right)}$$

$$r_{C_nH_{2n+2}} = \frac{k_A P_{H_2} \prod_{j=1}^{n} \alpha_j}{1 + \left(1 + \frac{1}{K_a K_b K_c}\frac{P_{H_2O}}{P_{H_2}} + \frac{1}{K_b K_c}\frac{1}{P_{H_2}} + \frac{1}{K_c}\right) \sum_{m=1}^{N} \left(\prod_{j=1}^{m} \alpha_j\right)}$$

$$r_{C_nH_{2n}} = \frac{k_B (1-\beta_n) \prod_{j=1}^{n} \alpha_j}{1 + \left(1 + \frac{1}{K_a K_b K_c}\frac{P_{H_2O}}{P_{H_2}} + \frac{1}{K_b K_c}\frac{1}{P_{H_2}} + \frac{1}{K_c}\right) \sum_{m=1}^{N} \left(\prod_{j=1}^{m} \alpha_j\right)}$$

$$r_{CO_2} = \frac{k_\upsilon (P_{CO} P_{H_2O}/P_{H_2}^{0.5} - P_{CO_2} P_{H_2}^{0.5}/K_p)}{1 + K_\upsilon P_{CO} P_{H_2O}/P_{H_2}^{0.5}}$$

$$\alpha_1 = \frac{k_1 P_{CO}}{k_1 P_{CO} + k_{AM} P_{H_2}} \text{ (for } n = 1);$$

$$\alpha_n = \frac{k_1 P_{CO}}{k_1 P_{CO} + k_A P_{H_2} + k_B (1-\beta_n)} \text{ (for } n \geq 2)$$

$$\alpha_{ASF} = \frac{k_1 P_{CO}}{k_1 P_{CO} + k_A P_{H_2} + k_B};$$

$$\beta_n = \frac{k_{-B}}{k_B} \frac{P_{C_nH_{2n}}}{\alpha_{ASF}^{n-1} \frac{k_1 P_{CO}}{k_1 P_{CO} + k_A P_{H_2}} + \frac{k_{-B}}{k_1 P_{CO} + k_A P_{H_2} + k_B} \sum_{m=2}^{n} \alpha_{ASF}^{m-2} P_{C_{(n-m+2)}H_{2(n-m+2)}}}$$

$$k_m(T) - k_{m,0} \exp(-E_m/RT)$$

Parameter Values:

$k_1 = 2.23 \times 10^{-7}$ mol/kg$_{catalyst}$ Pa s
$k_{AM,0} = 4.65 \times 10^{1}$ mol/kg$_{catalyst}$ Pa s
$E_{AM} = 92.89 \times 10^{3}$ J/mol
$k_{A,0} = 2.74$ mol/kg$_{catalyst}$ Pa s
$E_A = 87.01 \times 10^{3}$ J/mol
$k_{B,0} = 2.66 \times 10^{9}$ mol/kg$_{catalyst}$ s
$E_B = 11.10 \times 10^{4}$ J/mol
$k_{\upsilon,0} = 4.96 \times 10^{-4}$ mol/kg$_{catalyst}$ Pa$^{-1.5}$ s
$E_\upsilon = 45.08 \times 10^{3}$ J/mol
$k_{-B} = 2.75 \times 10^{-7}$ mol/kg$_{catalyst}$ Pa s
$K_\upsilon = 3.57 \times 10^{-6}$ Pa$^{-0.5}$
$K_a = 1.81 \times 10^{-2}$
$K_b = 4.68 \times 10^{-2}$
$K_c = 2.26 \times 10^{-1}$

$$k_p = \exp\left[-13.148 + \frac{5639.5}{T} + 1.077 \ln T + 5.44 \times 10^{-4} T - 1.125 \times 10^{-7} T^2 - \frac{49170}{T^2}\right]$$

triangular elements in each solution, which provide similar results to the ones involving higher number of grid points, but at a shorter execution time.

Default dimensions and properties of the unit cell as well as inlet properties of the reaction mixture and cooling fluid are given in Table 4. In order to conduct the parametric analyses, thickness and material type of the wall separating the channels, side length of the cooling channel, superficial velocity of the cooling fluid, and texture of the channel walls are changed on a systematic basis. The parameter under investigation is changed according to the values given in Table 5, whereas remaining parameters are kept at their default values listed in Table 4.

Results and Discussions

Results of the parametric analyses are given in Figures 2–5 and in Figure 7 in terms of temperature profile along the centerline of the reaction channel. Temperatures reported in parenthesis within the figures are averages of the pertinent profile, which are calculated by integrating temperature values at the centerline over the channel length and dividing it by the channel length.

The effect of thickness of the wall between the channels on reaction temperature is shown in Figure 2. It can be observed that the maximum temperature in the reaction channel increases as the wall thickness decreases. This trend can be discussed through conduction parameter, λ, a dimensionless number which is used to compare the significance of heat conduction within the wall with the heat carried by the fluid[21]:

$$\lambda = k_w A_c / m_f C_{Pf} L \tag{4}$$

Conduction parameter related to the fluid in the reaction channel is found to increase with wall thickness; the λ values are calculated as 3.08, 4.62, 6.16, 7.70, and 9.24 for the wall thicknesses of 2, 3, 4, 5, and 6×10^{-4} m, respectively. Such an increase indicates higher amounts of heat loss from the reaction channel, because conduction parameter is a measure showing how much of available energy can be transferred through the wall via axial conduction (in x-direction); the A_c term in the numerator of Eq. 4 is the product of wall thickness (in y-direction) with unit depth (in z-direction) of the unit cell (Figure 1) and indicates conductive heat flow perpendicular to it. Increase in the axial conduction leads to effective heat removal as the counter-flowing steam absorbs more energy from the upstream zones of the reaction channel and reduces the rate of exothermic reactions accompanied with dampened peak, channel exit, and average temperatures (Figure 2). Temperature profiles also show that the distance between the exit of the reaction channel (or the entrance of the cooling channel) and the locus of the maximum temperature increase

Table 3. Boundary Conditions Related to the Equations in Table 1

Channel inlets		
Reaction channel,	$x = L$	$u_1 = u_1^{in};\ c_{j,1} = c_{j,1}^{in};\ T_1 = T_1^{in}$
Cooling channel,	$x = 0$	$u_2 = u_2^{in};\ T_2 = T_2^{in}$
Channel outlets		
Reaction channel,	$x = 0$	$p_1 = p_1^{out};\ \mathbf{n} \cdot (-D_{AB} \nabla c_{j,1}) = 0;$ $\mathbf{n} \cdot (-k_{f,1} \nabla T_1) = 0$
Cooling channel,	$x = L$	$p_2 = p_2^{out};\ \mathbf{n} \cdot (-k_{f,2} \nabla T_2) = 0$
Line of symmetry (center-line of the channels, Figure 1)		
Reaction channel		$\mathbf{n} \cdot \mathbf{v}_1 = 0;\ \mathbf{n} \cdot (-D_{AB} \nabla c_{j,1} + \mathbf{v}_1 . c_{j,1}) = 0;$ $\mathbf{n} \cdot (-k_{f,1} \nabla T_1 + \mathbf{v}_1 \rho_{f,1} C_{Pf,1} T_1) = 0$
Cooling channel		$\mathbf{n} \cdot \mathbf{v}_2 = 0;\ \mathbf{n} \cdot (-k_{f,2} \nabla T_2 + \mathbf{v}_2 \rho_{f,2} C_{Pf,2} T_2) = 0$
Fluid-solid wall interface		
Reaction channel		$\mathbf{n} \cdot \mathbf{v}_1 = 0;\ \mathbf{n} \cdot (-D_{AB} \nabla c_{j,1} + \mathbf{v}_1 . c_{j,1}) = 0$ $\mathbf{n} \cdot (-k_{f,1} \nabla T_1 + \mathbf{v}_1 \rho_{f,1} C_{Pf,1} T_1) = \mathbf{n} \cdot (-k_w \nabla T_w)$
Cooling channel		$\mathbf{n} \cdot \mathbf{v}_2 = 0;$ $\mathbf{n} \cdot (-k_{f,2} \nabla T_2 + \mathbf{v}_2 \rho_{f,2} C_{Pf,2} T_2) = \mathbf{n} \cdot (-k_w \nabla T_w)$
Solid wall boundaries at $x = 0$ and $x = L$		$\mathbf{n} \cdot (-k_w \nabla T_w) = 0$

Table 4. Default Values of Microreactor Configuration and the Feed Conditions

Microreactor Configuration		Feed Conditions	
Side length of the reaction channel	5×10^{-4} m	Molar H_2:CO ratio	2.0
Thickness of the catalytic washcoat	5×10^{-5} m	Total reactant molar flow rate	4.8×10^{-4} mol/s
Thickness of the separating wall	3×10^{-4} m	Superficial velocity—both channels	5 m/s
Side length of the cooling channel	6×10^{-4} m	Temperature/reaction channel	623 K
Channel length	2×10^{-1} m	Temperature/cooling channel	374 K
Wall material	AISI Steel	Pressure/reaction channel	2×10^{6} Pa
Cooling fluid	Steam	Pressure/cooling channel	1×10^{5} Pa

with wall thickness. Location of the peak is moved inward to the left by the pronounced effect of axial heat conduction that favors energy interaction between the channels. These observations are similar to the studies involving different wall separated endothermic–exothermic flow couplings which report that the amount of heat transfer through the wall increases with wall thickness.[22–24]

In addition to its thickness, type of wall material is investigated in terms of its impact on the reaction temperature. For this purpose, use of four different materials—alumina, AISI steel, aluminum, and copper—having different thermal conductivities listed in Table 5 are simulated. At this point, it is worth noting that mechanical properties of copper and aluminum may limit their practical use at high temperature and pressure applications. However, because of their thermal conductivities which are significantly above those of alumina and steel, aluminum and copper are considered in this study for a clear parametric understanding of the effect of wall thermal conductivity on reactor operation. The results presented in Figure 3 show that as thermal conductivity of the material increases, maximum temperature in the reaction channel decreases and temperature profile becomes flatter. As in the analysis of wall thickness, the effect of material type can be explained by the conduction parameter defined in Eq. 4. Values of λ based on fluid mixture in the reaction channel are found to be 2.80, 4.62, 20.9, and 41.6 for alumina, AISI steel, aluminum, and copper, respectively, showing that axial conduction becomes more pronounced with thermal conductivity. In the case of alumina, exothermal heat is preserved within the channel rather than being dissipated into the wall and, therefore, temperature rise becomes more notable, resulting with maximum, average and exit values of ca. 683 K, 650 K, and 613 K, respectively. On the other extreme, copper is highly capable of conducting heat to the cooling channel that sweeps the exothermal heat as soon as it is released and reduces the maximum, average, and exit temperatures down to ca. 648 K, 624 K, and 500 K, respectively (Figure 3). These findings are in accordance with those of similar studies in the literature stating that the maximum and average temperatures of reaction channel will be higher when using materials with low conductivity.[22–24] Apart from temperature, distance of the locus of peak temperature from the entrance of the reaction channel is found to increase with thermal conductivity. This is due to the fact that the reaction mixture is forced to transfer its heat to steam before reactions move forward and release more heat.

The effects of side length of the square-shaped cooling microchannel on the temperature of the reaction stream are also simulated. To make sure that constant mass flow rate of steam is fed in every simulation, linear velocity is changed accordingly (Table 5) together with the side length. Resulting temperature profiles are presented in Figure 4. It can be observed that as side length of the cooling channel is changed from 7×10^{-4} m to 4×10^{-4} m by increments of 1×10^{-4} m, the maximum and average temperatures in the reaction channel are found to increase. Considering that mass flow is constant, the effect of geometric change is reflected by the superficial (linear) velocity of steam, which is inversely proportional to the hydraulic diameter. Superficial velocity is important as it determines the residence time of cooling fluid within the reactor. In the case of bigger cooling channel diameters, steam spends more time in the channel and has the opportunity to absorb more exothermal heat, which is the main reason of having lower peak and average temperatures; the opposite is valid for smaller channel openings. The reaction exit temperature, however, follows a somewhat different trend, and is proportional to the side length (Figure 4). A possible explanation of this observation can be made by the coolant-side heat transfer coefficient at the entrance of the cooling channel. Although the flow is laminar in microchannels, mixing can improve the heat-transfer coefficient at the so-called "entry zones" in which the flow is not fully developed yet.[25] Because of this phenomenon, it can be speculated that high superficial steam velocities help in drawing more heat from the exit of the reaction channel and reducing its temperature. This explanation also brings insight into the shift of the location of peak temperature. As its mass flow rate is constant in all cases, portion of the cooling capacity of steam used at the

Table 5. Values Studied in Parametric Analyses

Wall thickness ($\times 10^6$ m)	200, 300, 400, 500, 600			
Wall material[1]	Alumina (27), AISI Steel (44.5), aluminum (201), copper (400)			
Side length of the cooling channel ($\times 10^6$ m)[2]	400 (11.3), 500 (7.2), 600 (5.0), 700 (3.5)			
Superficial velocity of steam (m/s)	5, 10, 15, 20			
Channel texture	Type	I	II	III
	W_b ($\times 10^3$ m)	5	5	5
	L_b ($\times 10^6$ m)	150	150	150
	Location	Reaction channel	Both channels	Cooling channel

[1]Thermal conductivity of each material in units of W/m K is given in parenthesis.
[2]Superficial velocities (in units of m/s) that are calculated to give constant mass flow rate of steam are given in parenthesis.

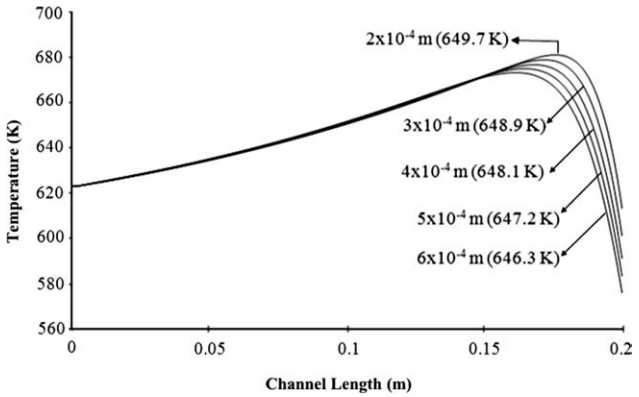

Figure 2. Effect of thickness of the wall separating the channels on temperature of the FT reaction channel.

Simulated wall thickness values ($\times 10^4$ m) = 2, 3, 4, 5, 6. Refer to Table 4 for the values of other geometric and operational parameters. Average channel temperatures are shown in parentheses.

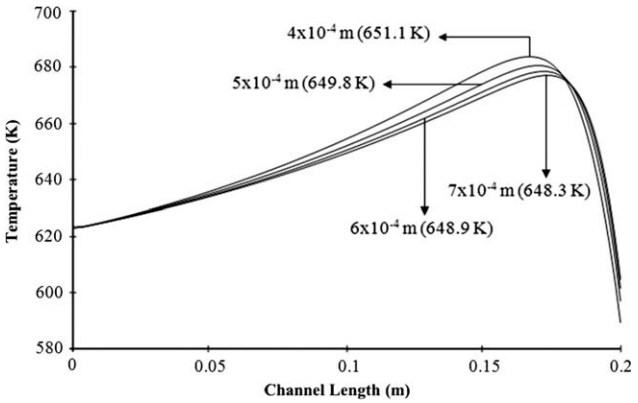

Figure 4. Effect of side length of the square-shaped cooling channel on temperature of the FT reaction channel.

Simulated side length values ($\times 10^4$ m) = 4, 5, 6, 7. Refer to Table 4 for the values of other geometric and operational parameters. Average channel temperatures are shown in parentheses.

cooling inlet/reaction exit zone due to the mixing effect is bigger in the case of smaller side lengths. The pronounced cooling causes the temperature peak to occur in the inner parts of the reaction channel, as observed in Figure 4. The effect of decreasing side length on pressure drop is also addressed and found to be negligible; it is calculated as 3.6×10^3 Pa for the smallest side length of 4×10^{-4} m.

Superficial velocity of steam is studied as a different parameter due to its importance in reactor operation explained above. For this purpose, side length of the cooling channel is kept constant at 6×10^{-4} m, but the steam velocities are changed from 5 to 20 m/s as outlined in Table 5. Outcomes of these simulations are given in Figure 5. The profiles show that increasing linear velocity of steam in the 5–10 m/s range results in slight elevations in maximum and average temperatures of the reaction channel, ca. by 4 K and 1.4 K, respectively, both of which then decrease significantly (by ca. 41 K and 52 K, respectively) in the 10–20 m/s range. As increasing the velocity at constant side length (i.e., hydraulic diameter) corresponds to higher rates of mass flow, it improves the cooling capacity of the steam and enables it to draw more heat from reaction channel; this is the reason of having significant temperature reductions in the 10–20 m/s range. However, in the 5–10 m/s range, this phenomenon is slightly suppressed by the improvement of the cooling-side heat transfer coefficient due to mixing, the phenomenon explained above. In other words, increase in steam velocity is significant enough to draw heat at the cooling inlet/reaction exit zone at a big portion such that the cooling capacity of steam is reduced for the remainder of the channel, causing slight elevations in the maximum and average reaction temperatures. Increasing steam flow rate is also evaluated in terms of pressure drop along the cooling channel, which is calculated as 2.9×10^3 Pa for the 20 m/s steam flow. Considering that pressure drop in the default case, i.e., 5 m/s steam flow, is 6.9×10^2 Pa, it can be

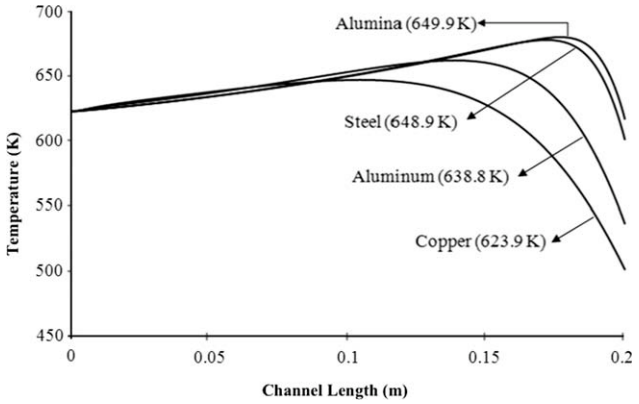

Figure 3. Effect of material type of the wall separating the channels on temperature of the FT reaction channel.

Simulated wall material types = alumina (k_w = 27 W/m K), AISI Steel (k_w = 44.5 W/m K), aluminum (k_w = 201 W/m K), copper (k_w = 400 W/m K). Refer to Table 4 for the values of other geometric and operational parameters. Average channel temperatures are shown in parentheses.

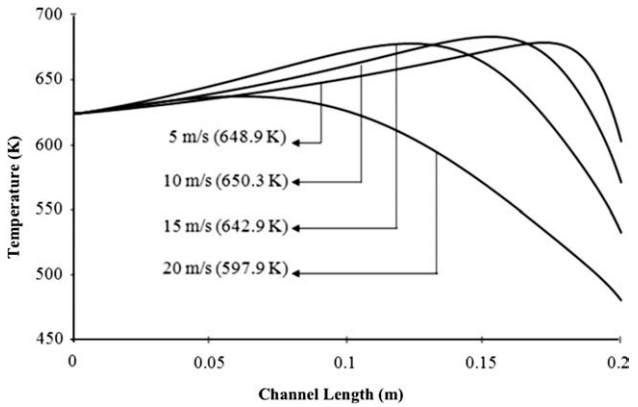

Figure 5. Effect of superficial velocity of steam on temperature of the FT reaction channel.

Simulated superficial steam velocity values (m/s) = 5, 10, 15, 20. Refer to Table 4 for the values of other geometric and operational parameters. Average channel temperatures are shown in parentheses.

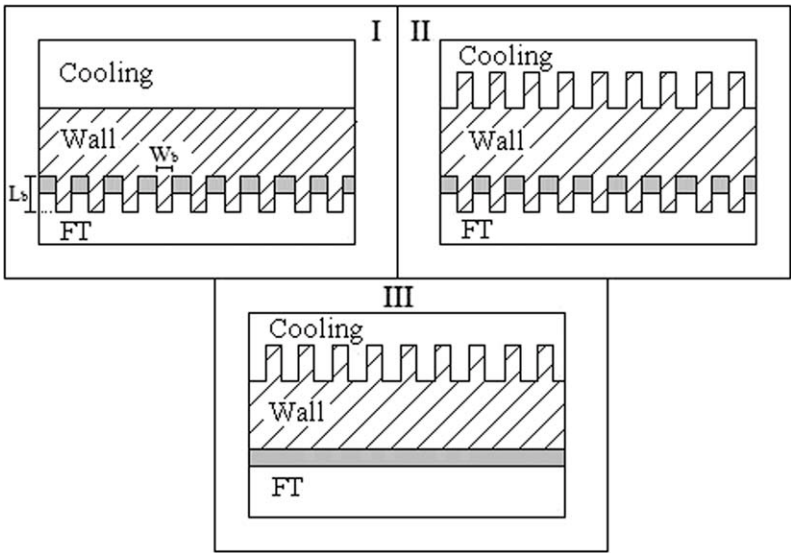

Figure 6. Geometric configurations of the channel wall textures.

Metal wall zones have been represented by dashed regions.

concluded that higher steam flow rates did not lead to any notable elevations in pressure drop.

Wall texture is studied as the final parameter to explore its impacts on the reaction channel temperature and is represented by the use of micro-baffles, the repeating rectangular patterns on the channel walls. These patterns are placed either to the reaction channel only (Type I) or to the cooling channel only (Type III) or to both of them (Type II), as shown in Figure 6. Effect of using micro-baffles on the cooling side is investigated by comparing (a) default case of the unit cell (straight walls in both channels) with Type III and (b) Type I with Type II, while comparison of the default case with Type I allows the observation of using rectangular patterns on the catalytic wall. Dimensions of the micro-baffles used in Types I, II, and III are given in Table 5.

Figure 7 shows the temperature profiles of the reaction channels obtained for the unit cell configurations defined in Figure 6. It can be observed that the difference between the default unit cell geometry and the one having micro-baffles only in the cooling channel (Type III) is very small; temperature profiles obtained for both cases are almost overlapping. Similarly, the profiles obtained for Types I and II do not differ from each other. Considering these results, it can be inferred that using micro-baffles in the cooling channel does not bring notable changes into the reaction temperature. When micro-baffles are used in the reaction channel, however, the shift in the temperature profile is more obvious (default case vs. Type I) leading to ca. 11.6 K of reduction in average channel temperature. This change can be attributed to the role of micro-baffles in heat transfer; these patterns act as static-mixers, i.e., induce mixing in the channel where flow is laminar and helps improving the local heat transfer coefficient between the catalytic washcoat and the solid wall. As a result, generated heat is transferred to the wall more effectively, leading to lower temperatures as shown in Figure 7. The overall impact is more notable when baffles are used in reaction side rather than the cooling side, as the heat source, i.e., the catalyst is buried in the former side. The presence of micro-baffles in the reaction channel also leads to temperature profiles which are not smooth (Types I and II curves in Figure 7); the evolution of small temperature fluctuations are in accordance with the ''periodic'' location of the catalytic washcoat layers in the axial direction (Types I and II geometries in Figure 6). Although local temperature shifts may disturb product distribution, magnitudes of the fluctuations are very small and do not limit the use of baffled-textures in the reaction channel. Heat transfer enhancement by using patterns of static mixing in microchannels is reported also by other studies in the literature.[12,26,27] Myrstad et al.[12] have shown that use of pillar-shaped structured catalyst foils in FTS favored effective transfer of exothermal heat from the catalyst to the heat

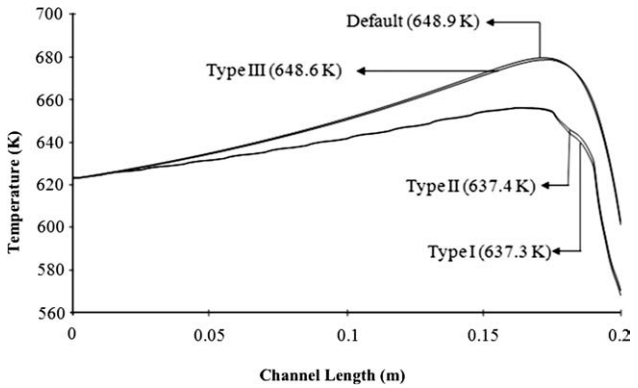

Figure 7. Effect of different channel wall textures on temperature of the FT reaction channel.

Refer to Table 4 for the values of geometric and operational parameters and Table 5 for the detailed definition of channel wall textures. Average channel temperatures are shown in parentheses.

transfer oil flowing in adjacent channels. Effect of using of micro-baffles on pressure drop is also studied. For this purpose, Type I configuration (Figure 6) is compared with the default unit cell shown in Figure 1. It is found that the presence of micro-baffles in the reaction channel increases the pressure drop (1.5×10^2 Pa and 4.9×10^1 Pa, with and without baffles, respectively). Nevertheless, the increase is not significant to prevent the use of nonstraight configurations in microchannel reactors, which is also confirmed by the results reported in the literature.[12,26,27]

In addition to the parametric changes discussed above, the effect of direction of coolant and reactive streams on reaction temperature is also studied. For this purpose, the streams are set to flow in the same direction, i.e., in the co-current flow mode and the system is simulated according to the parameters listed in Table 4. It is observed that, due to the very high heat transfer rates involved in the micro-geometry, reaction did not proceed due to the immediate cooling introduced by the coolant in the neighboring channels; reactive stream is almost quenched (by the coolant) before the start-up of the reaction. The same outcome is obtained when parametric changes mentioned in Table 5 are applied. As a result, the co-current configuration is found to be infeasible, as it prevented the initiation and progress of FTS at the specified conditions.

It is worth noting that the findings above should be coupled with actual process considerations for designing intensified FTS reactors. In addition to its thermal conductivity, reactor material should be able to withstand high pressures of FT operation, corrosion, as well as high temperatures in case of cooling problems such as partial or complete blocking of the cooling channels due to fouling. Considering these facts, stainless steel seem to be a proper choice of material, as it can provide acceptable thermal conductivity performance together with the possibility of improvement of mechanical, thermal, and corrosion resistances via addition of relevant ingredients. Cooling channel size, which is found to have minimal effect on temperature control, can be selected at the highest possible value (e.g., 7×10^{-4} m in this study), as wider channels will not get fouled as quick as the narrow ones plus they will allow higher coolant flow rates for removing scales with less pressure drop. In addition to improved temperature control, using thicker walls, e.g., higher than 7×10^{-4} m, can be preferred for providing inherent safety against thickness decrease due to corrosion as well as better mechanical durability against high pressures of FT reaction. The pressure difference between the channels should also be considered; the values studied in this work—2×10^6 Pa and 1×10^5 Pa in the FT and cooling channels, respectively—can end up with a significant pressure gradient. However, in actual operations, this problem may be overcome by using high-pressure steam, which is available in most of the production facilities, in the cooling channel. In addition, separating walls can be designed thick enough to resist any possible deformations.

Conclusions

The possibility of controlling the exothermal heat release of high-temperature FTS in a heat-exchanged, steam-cooled microchannel reactor is investigated through a computer-based parametric analysis involving changes in the reactor geometry and in operating conditions. The results show that using thicker channel-separating walls made of materials with high thermal conductivity may provide isothermal conditions for the FT operation. It is also observed that changing the side length of cooling channel has the least significant effect in terms of thermal response, whereas changing superficial velocity of steam can provide notable control over FT temperature; its average may even be forced to fall below feed temperature in case of excessive flow of the coolant. Changing the texture of the catalyst-coated wall by the use of micro-baffles is found to reduce peak and average reaction channel temperatures, showing possibility of their control, whereas these values remain almost unchanged when the baffled-texture is placed on the wall of cooling channel. In all cases, pressure drop is calculated to be at negligible values. These findings, however, should be considered together with actual process conditions and limitations in the design and manufacture of intensified heat-exchange integrated FTS reactors.

Acknowledgments

Financial support is provided by Bogazici University Research Fund through project BAP-09HA507D. Ahmet K. Avci thanks TUBA-GEBIP program.

Notation

A_c = cross-sectional area of the solid wall (m^2)
$c_{j,1}$ = concentration of species j in reaction channel (mol/m^3)
$C_{Pf,i}$ = specific heat of fluid in channel i (J/kg K)
$D_{AB,1}$ = diffusion coefficient of A in B (m^2/s)
$D_{AB,eff}$ = effective diffusion coefficient in the washcoat layer (m^2/s)
E_A = activation energy for paraffin formation (J/mol) ($n \geq 2$)
E_{AM} = activation energy for methane formation (J/mol)
E_B = activation energy for olefin formation (J/mol) ($n \geq 2$)
E_υ = activation energy for WGS reaction (J/mol)
$-\Delta H_m$ = enthalpy of reaction m (J/mol)
k_1 = rate constant of CO adsorption ($mol/kg_{catalyst}$ Pa s)
k_A = rate constant of paraffin formation ($mol/kg_{catalyst}$ Pa s)
k_{AM} = rate constant of methane formation ($mol/kg_{catalyst}$ Pa s)
k_B = rate constant of olefin desorption reaction ($mol/kg_{catalyst}$ s)
k_{-B} = rate constant of olefin readsorption reaction ($mol/kg_{catalyst}$ Pa s)
k_υ = rate constant of CO_2 formation ($mol/kg_{catalyst}$ $Pa^{-1.5}$ s)
$k_{m,0}$ = pre-exponential factor of rate constant of reaction m (unit same as of rate constant of reaction m)
k_{eff} = effective fluid thermal conductivity in the washcoat layer (W/m K)
$k_{f,i}$ = thermal conductivity of the fluid in channel i (W/m K)
k_w = thermal conductivity of the solid wall (W/m K)
K_a, K_b, K_c = equilibrium constants of elementary reaction steps in FTS
K_p = equilibrium constant of WGS reaction
K_υ = group of constants in WGS reaction ($Pa^{-0.5}$)
L = length of the unit cell (m)
L_b = length of micro-baffles (m)
m_f = mass flow rate of the fluid (kg/s)
n = number of carbon atoms
$\mathbf{n}$ = normal unit vector
p_i = pressure in channel i (Pa)
P_j = partial pressure of species j (Pa)
r_j = rate of formation of species j ($mol/kg_{catalyst}$ s)
r_m = rate of reaction m ($mol/kg_{catalyst}$ s)
R = gas constant (= 8.314 J/mol K)
$R_{j,1}$ = total rate of generation/depletion of species j in channel 1 ($mol/kg_{catalyst}$ s)
T_i = temperature of the fluid within channel i (K)
T_w = temperature of the solid wall (K)

u_i = superficial velocity into channel i (m/s)
$\mathbf{v}_i$ = fluid velocity vector in channel i, (m/s)
$v_{x,i}$ = x-component of linear fluid velocity in channel i (m/s)
$v_{y,i}$ = y-component of linear fluid velocity in channel i (m/s)
W_b = width of micro-baffles (m)
x_i = axial coordinate in channel i (m)
y_i = direction normal to the x-axis in channel i (m)

Greek letters

α_1 = chain growth factor for carbon number of 1
α_{ASF} = chain growth probability in the Anderson–Schulz–Flory distribution
α_n = chain growth factor for carbon number of n ($n \geq 2$)
β_n = readsorption factor of 1-olefin with carbon number of n
ε_p = porosity of the washcoat layer
κ = permeability of the washcoat layer (m^2)
λ = conduction parameter
μ_1 = fluid viscosity in the reaction channel (kg/m s)
$\rho_{f,i}$ = fluid density in channel i (kg/m^3)
ρ_s = density of the catalytic washcoat (kg/m^3)

Subscripts and superscripts

i = channel index (1 = reaction channel; 2 = cooling channel)
in = channel inlet
j = species index
m = reaction index
out = channel outlet
s = catalytic washcoat phase
w = solid wall phase

Literature Cited

1. Dry ME. Fischer–Tropsch reactions and the environment. *Appl Catal A*. 1999;189:185–190.
2. Dry ME. The Fischer–Tropsch process: 1950–2000. *Catal Today*. 2002;71:227–241.
3. Schulz H. Short history and present trends of Fischer–Tropsch synthesis. *Appl Catal A*. 1999;186:3–12.
4. Van der Laan GP, Beenackers AACM. Kinetics and selectivity of the Fischer Tropsch synthesis: a literature review. *Catal Rev Sci Eng*. 1999;41:255–318.
5. Aasberg-Petersen K, Christensen TS, Dybkjaer I, Sehested J, Ostberg M, Coertzen RM, Keyser MJ, Steynberg AP. *Synthesis gas production for FT synthesis*. In: Steynberg A, Dry ME, editors. *Fischer Tropsch Technology*. Amsterdam: Elsevier, 2004:258–405.
6. Steynberg AP. *Introduction to Fischer-Tropsch technology*. In: Steynberg A, Dry ME, editors. *Fischer Tropsch Technology*. Amsterdam: Elsevier, 2004:1–63.
7. Kolb G, Hessel V. Micro-structured reactors for gas phase reactions. *Chem Eng J*. 2004;98:1–38.
8. Kiwi-Minsker L, Renken A. Microstructured reactors for catalytic reactions. *Catal Today*. 2005;110:2–14.
9. Karakaya M, Avci AK. Comparison of compact reformer configurations for on-board fuel processing. *Int J Hydrogen Energy*. 2010;35:2305–2316.
10. Cao C, Hu J, Li S, Wilcox W, Wang Y. Intensified Fischer–Tropsch synthesis process with microchannel catalytic reactors. *Catal Today*. 2009;140:149–156.
11. Guillou L, Paul S, Le Courtois V. Investigation of H_2 staging effects on CO conversion and product distribution for Fischer–Tropsch synthesis in a structured microchannel reactor. *Chem Eng J*. 2008;136:66–76.
12. Myrstad R, Eri S, Pfeifer P, Rytter E, Holmen A. Fischer-Tropsch synthesis in a microstructured reactor. *Catal Today*. 2009;147S:S301–S304.
13. Arzamendi G, Diéguez PM, Montes M, Odriozola JA, Falabella Sousa-Aguiar E, Gandía LM. Computational fluid dynamics study of heat transfer in a microchannel reactor for low-temperature Fischer–Tropsch synthesis. *Chem Eng J*. 2010;160:915–922.
14. Avci AK, Trimm DL, Karakaya M. Microreactor catalytic combustion for chemicals processing. *Catal Today*. 2010;155:66–74.
15. Shen WJ, Zhou JL, Zhang BJ. Intraparticle diffusion effects in Fischer-Tropsch synthesis. I. Modeling of diffusion and reaction. *J Nat Gas Chem*. 1996;5:59–68.
16. Poling BE, Prausnitz JM, O'Connell JP. *The Properties of Gases and Liquids*, 5th ed. New York: McGraw Hill, 2001.
17. Rase HF. *Fixed-Bed Reactor Design and Diagnostics*. Massachusetts: Butterworths, 1990.
18. Smith JM, Van Ness HC, Abbott MM. *Introduction to Chemical Engineering Thermodynamics*, 7th ed. Singapore: McGraw Hill, 2005.
19. Geankoplis CJ. *Transport Processes and Separation Process Principles*, 4th ed. New Jersey: Prentice Hall, 2003.
20. Wang YN, Ma WP, Lu YJ, Yang J, Xu YY, Xiang HW, Li YW, Zhao YL, Zhang BJ. Kinetics modelling of Fischer–Tropsch synthesis over an industrial Fe–Cu–K catalyst. *Fuel*. 2003;82:195–213.
21. Peterson RB. Numerical modeling of conduction effects in microscale counterflow heat exchangers. *Microscale Thermophys Eng*. 1999;3:17–30.
22. Norton DG, Vlachos DG. Combustion characteristics and flame stability at the microscale: a CFD study of premixed methane/air mixtures. *Chem Eng Sci*. 2003;58:4871–4882.
23. Norton DG, Vlachos DG. A CFD study of propane/air microflame stability. *Combust Flame*. 2004;138:97–107.
24. Stutz MJ, Poulikakos D. Effects of microreactor wall heat conduction on the reforming process of methane. *Chem Eng Sci*. 2005;60:6983–6997.
25. Hoebink JHBJ, Harmsen JMA, Scholz CML, Marin GB, Schouten JC. *Modeling of automotive exhaust gas converters*. In: Cybulski A, Moulijn JA, editors. *Structured Catalysts and Reactors*. Boca Raton: CRC Press, 2006:311–354.
26. Hardt S, Ehrfeld W, Hessel V, Vanden Bussche KM. Strategies for size reduction of microreactors by heat transfer enhancement effects. *Chem Eng Commun*. 2003;190:540–559.
27. Karakaya M, Avci AK. Simulation of on-board fuel conversion in catalytic microchannel reactor-heat exchanger systems. *Top Catal*. 2009;52:2112–2116.

Manuscript received Sep. 25, 2010, and revision received Jan. 9, 2011.